

1 Future changes in seasonal climate predictability

2

3 Dillon J. Amaya<sup>1</sup>, Nicola Maher<sup>2,3,4</sup>, Clara Deser<sup>5</sup>, Michael G. Jacox<sup>1,6</sup>, Michael A. Alexander<sup>1</sup>,  
4 Matthew Newman<sup>1</sup>, Juliana Dias<sup>1</sup>, and Jiale Lou<sup>7</sup>

5

6 <sup>1</sup>Physical Science Laboratory, National Oceanic and Atmospheric Administration, 325  
7 Broadway, Boulder, CO 80305, USA

8 <sup>2</sup>Cooperative Institute for Research in Environmental Sciences, University of Colorado  
9 Boulder, 216 UCB, University of Colorado Boulder campus, Boulder, CO 80309, USA

10 <sup>3</sup>Department of Atmospheric and Oceanic Sciences (ATOC), University of Colorado at  
11 Boulder, Boulder, CO 80309, USA

12 <sup>4</sup>Australian National University and ARC Centre of Excellence for Climate Extremes,  
13 Canberra, ACT 0200, Australia

14 <sup>5</sup>National Center for Atmospheric Research, 1850 Table Mesa Dr, Boulder, CO 80305, USA

15 <sup>6</sup>Environmental Research Division, Southwest Fisheries Science Center, National Oceanic  
16 and Atmospheric Administration, 99 Pacific St #255A, Monterey, CA 93940, USA

17 <sup>7</sup>Atmospheric and Oceanic Sciences Program, Princeton University, Princeton, NJ, USA

18

19

20

21

22

23 Corresponding author: Dillon J. Amaya, [dillon.amaya@noaa.gov](mailto:dillon.amaya@noaa.gov), 816-916-8348

24

25 **Abstract**

26 Seasonal forecasts provide critical decision support tools for managing important  
27 socioeconomically-relevant resources. As the result of continued model development, the skill of  
28 such tools has improved over the years. However, further advancements are hampered by the  
29 climate's "potential predictability", an upper limit for how accurately we can predict different  
30 parameters that is intrinsic to the chaotic nature of the climate system. Recent studies have shown  
31 that potential predictability and actual forecast skill have varied throughout the historical record,  
32 primarily as a result of natural decadal variability. In this study, we explore whether potential  
33 predictability will change in the future as a distinct response to anthropogenic climate change. We  
34 quantify the potential predictability limits of the El Niño-Southern Oscillation (ENSO) as well as  
35 global surface temperature, precipitation, and upper atmospheric circulation anomalies from 1921-  
36 2100 by applying a perfect model framework to five coupled model large ensembles. We find that  
37 the sign, magnitude, and timing of predictability changes are highly model dependent, with some  
38 producing a robust increase or decrease in potential predictability by 2100, and others producing  
39 no significant change. While there is large intermodel uncertainty in future predictability changes,  
40 a common physical mechanism emerges that allows us to anticipate how real-world predictability  
41 may change in the coming decades. In particular, predictability changes in each model are strongly  
42 linked to their projected change in ENSO amplitude. Therefore, historical forecast skill  
43 relationships that depend on ENSO and its teleconnections may be altered as the climate continues  
44 to change.

## 45 **1. Introduction**

46           Seasonal climate forecasts provide important decision support tools to help stakeholders  
47 manage a variety of socioeconomically-relevant resources. For example, initialized dynamical  
48 forecasts are routinely used to provide seasonal outlooks of regional precipitation and surface  
49 temperature, tropical cyclone activity, and climate modes such as the El Niño-Southern Oscillation  
50 (ENSO). While recent advances in model physics, resolution, ensemble sizes, and data  
51 assimilation schemes have led to increases in seasonal forecast skill (Barnston et al. 2012; Barnston  
52 and Tippett 2017), prediction systems are still limited by the so-called “potential predictability” of  
53 different climate parameters. Potential predictability is a hard predictability limit intrinsic to the  
54 chaotic nature of the climate system (Sardeshmukh et al. 2000), a limit that most traditional  
55 dynamical forecasts often fail to reach due to the presence of model errors. As a result of this  
56 ceiling, further reduction of model biases may yield only incremental increases in forecast skill as  
57 predictability limits are reached for different aspects of the climate system (Newman &  
58 Sardeshmukh, 2017).

59           However, there may still be opportunities to improve seasonal forecast systems. Recent  
60 studies have shown that potential predictability limits are not stationary or fixed in time (Newman  
61 & Sardeshmukh, 2017; Weisheimer et al., 2022; Zhao et al., 2016). As a result, actual forecast skill  
62 has also varied substantially in the past (Derome et al., 2005; Kumar, 2009; MacLeod et al., 2018;  
63 O’Reilly et al., 2017, 2019; Shi et al., 2015; Weisheimer et al., 2017, 2019). For example, Lou et  
64 al. (2023) and Weisheimer et al. (2022) showed that long-lead ENSO forecast skill was higher at  
65 the beginning and end of the twentieth century, with a multidecadal period of lower skill from the  
66 1930s-1950s. Further, Weisheimer et al. (2020) found that past seasonal predictability of  
67 extratropical atmospheric circulation patterns such as the Pacific-North American (PNA) pattern  
68 and the North Atlantic Oscillation (NAO) have also experienced pronounced decadal variations.  
69 While these past changes in prediction skill may result from varied model performance relative to  
70 historical observations (e.g., Weisheimer et al., 2022), these skill changes may also be driven by  
71 changes in the intrinsic predictability of the climate system itself (Becker et al. 2014; Newman and  
72 Sardeshmukh 2017).

73           Given these historical changes, it is reasonable to expect that potential predictability and  
74 actual prediction skill may similarly vary in the future, whether as a result of natural decadal  
75 variability (Weisheimer et al., 2020), a possible response to anthropogenic climate change (Zheng

76 et al. 2022), or some combination of both. In particular, some general circulation models (GCMs)  
77 project that ENSO and its remote impacts may change in response to an increase in greenhouse  
78 gasses (e.g., Cai et al., 2021). For example, some models project significant changes in ENSO  
79 variability (Maher et al. 2023; Heede and Fedorov 2023), frequency (Berner et al. 2020), flavor  
80 (i.e., central vs eastern Pacific; Capotondi et al., 2015), and teleconnection strength/position (Gan  
81 et al. 2017; McGregor et al. 2022; O'Brien and Deser 2023; Zhou et al. 2014). Although, there is  
82 substantial uncertainty in the sign and intensity of these changes across models. Nevertheless, due  
83 to its far-reaching teleconnections (e.g., Horel & Wallace, 1981), ENSO is the single most  
84 important source of predictability on seasonal timescales for much of the globe (e.g., Barnett &  
85 Preisendorfer, 1987; Jacox et al., 2019; Quan et al., 2006). Therefore, any future changes to  
86 ENSO's strength and/or its connectivity to the rest of the climate system could significantly impact  
87 the potential predictability of many socioeconomically-relevant climate parameters.

88         It is crucial to assess how potential predictability may evolve as climate continues to  
89 change. Many previous studies have used hindcast systems to estimate potential predictability in  
90 the past (e.g., Shi et al., 2015; Weisheimer et al., 2019, 2020, 2022). However, model hindcasts  
91 are not useful for quantifying possible future changes in predictability as they are by definition  
92 retrospective and depend on past observations for their initialization. A different technique that  
93 can overcome these limitations and assess time-varying climate predictability in the past and the  
94 future is the “model-analog” approach. In the traditional analog framework, past observed climate  
95 states are found that closely match the current state and their subsequent evolution are treated as  
96 forecasts (Lorenz 1969). Alternatively, coupled GCMs allow for analogs to be drawn from climate  
97 simulations (often pre-industrial control runs; Ding et al., 2018), with the model evolution of these  
98 analogs then treated as the forecast. This method increases the “library” of possible climate states  
99 to compare against the current observed state, resulting in closer analog matches and allowing for  
100 the generation of forecast ensembles. Such model-analog forecasts have been shown to be as  
101 skillful as initialized dynamical forecasts (Ding et al. 2018, 2019), with the added benefit of being  
102 more computationally efficient.

103         The “perfect model-analog” technique utilizes these same methods, but whereas the goal  
104 of a traditional model-analog is to leverage climate simulations to forecast the real world, the goal  
105 of the perfect model framework is to instead forecast the climate simulation itself. This is  
106 accomplished by treating a portion of a climate simulation as “observations”, and then drawing

107 the analog forecasts from a different, independent portion of the same climate simulation. The  
108 resulting ensemble forecast is “perfect” in that it has no unconditional or conditional biases (von  
109 Storch & Zwiers, 1999). Thus, the forecast skill in a perfect model framework is a measure of the  
110 potential predictability (or equivalently, “potential skill”) in the climate system. Since the perfect  
111 model framework does not depend on real world observations, it can be readily applied to past and  
112 future climate simulations to explore how these predictability limits change over time.

113 In this study, we quantify seasonal climate predictability limits from 1921-2100 by  
114 applying the perfect model framework to five coupled model initial condition large ensembles  
115 (LEs) that are each forced with time-varying radiative forcing. Model LEs have been widely used  
116 in climate science studies to separate the response to external forcing from internal climate  
117 variations (see review by Maher et al., 2021). In our analysis, the large number of ensemble  
118 members provided by each model LE (ranging from 30-100 depending on model) allows us to  
119 generate hundreds of thousands of perfect model forecasts with which to assess any future changes  
120 in potential predictability. In particular, we generate 24-month forecasts of global surface  
121 temperature, precipitation, and upper atmospheric circulation anomalies as well as for ENSO. The  
122 forecasts are then verified against independent portions of the same large ensembles using anomaly  
123 correlation coefficient (ACC) and reliability categories—a probabilistic measure of forecast skill.  
124 Finally, we relate future changes in potential predictability to future ENSO changes in each model.

125

## 126 **2. Data and Methods**

### 127 *(a) Climate model simulations and observations*

128 We apply the perfect model framework to five coupled model initial condition LEs that  
129 span the Coupled Model Intercomparison Project Phase 5 (CMIP5) and CMIP6 eras (Table 1).  
130 Such a comparison across models allows us to test the sensitivity of our results to inter-model  
131 uncertainty found in the climate response to increased radiative forcing. For efficiency, all model  
132 data output was first interpolated to a common  $2.5^\circ \times 2.5^\circ$  grid.

133 The models used in our analysis include: the Community Earth System Model version 1.2  
134 LE (CESM1-LE; 40 members; (Kay et al. 2015), CESM version 2 LE (CESM2-LE; 100 members;  
135 Rodgers et al., 2021), the Geophysical Fluid Dynamics Laboratory Seamless System for Prediction  
136 and Earth System Research Medium Resolution Simulation (GFDL-SPEAR; 30 members;  
137 Delworth et al., 2020), the GFDL Earth System Modeling version 2M (GFDL-ESM2M; 30

138 members; Burger et al., 2022), and the Max-Planck Institute Grand Ensemble (MPI-GE; 100  
 139 members; Maher et al., 2019). The analysis period is 1921-2100, during which each model uses a  
 140 specified external forcing scenario: (1) historical + retrospective emissions pathway 8.5 (RCP8.5),  
 141 (2) historical + shared socioeconomic pathway 3-7.0 (SSP3-7.0), or (3) historical + SSP5-8.5.  
 142

Dataset	Forcing (ens. size)	$\sigma_{3.4}$ trend ( $^{\circ}\text{C dec}^{-1}$ )	$\sigma_{3.4}$ trend ( $^{\circ}\text{C dec}^{-1}$ )	Reference
		1950-2022	1950-2100	
<b>CESM1-LE</b>	HIST+RCP8.5 (40)	$0.04 \pm 0.03$	$0.02 \pm 0.02$	Kay et al. (2015)
<b>CESM2-LE</b>	HIST+SSP3-7.0 (100)	$0.03 \pm 0.04$	$0.00 \pm 0.02$	Rodgers et al. (2021)
<b>GFDL-SPEAR</b>	HIST+SSP5-8.5 (30)	$0.02 \pm 0.03$	$0.03 \pm 0.01$	Delworth et al. (2020)
<b>GFDL-ESM2M</b>	HIST+RCP8.5 (30)	$0.02 \pm 0.05$	$-0.02 \pm 0.02$	Burger et al. (2022)
<b>MPI-GE</b>	HIST+RCP8.5 (100)	$0.00 \pm 0.04$	$0.00 \pm 0.01$	Maher et al. (2019)
<b>ERSSTv5</b>		0.03		Huang et al. (2017)

143 **Table 1** Observational and model datasets used in this study. First column: radiation forcing scenario used by  
 144 each model. The number of ensemble members available in each model is in parentheses. Second column:  
 145 December-February averaged Nino3.4 standard deviation ( $\sigma_{3.4}$ ) trend ( $^{\circ}\text{C decade}^{-1}$ ) in 30-year running windows  
 146 (i.e., Figure 1) for the period 1950-2022. For climate models, the ensemble mean trend is reported along with  
 147 +/- one standard deviation. Third column: As in the second column, but for the period 1950-2100. Fourth column:  
 148 Dataset references.  
 149

150 Within a given model, each ensemble member starts from a different initial condition. Over  
 151 time, the ensemble members diverge due to the chaotic nature of the coupled climate system. As  
 152 a result, once the memory of the initial condition fades, each ensemble member can be treated as  
 153 an independent sample of the climate that has its own unique sequence of internal variability  
 154 superimposed on a common forced response. We compare a portion of our model results to  
 155 monthly mean data from National Oceanic and Atmospheric Administration (NOAA) Extended  
 156 Reconstructed Sea Surface Temperature (SST) version 5 (ERSSTv5; Huang et al., 2017) from  
 157 1921-2022.

158  
 159 *(b) Perfect model-analog framework*

160 In each LE, perfect model forecasts are generated and evaluated for different 30-year  
 161 periods spaced every 10 years from 1921-2100 (e.g., 1921-1950, 1931-1960...2071-2100). The  
 162 forecasts are produced within each of these 30-year periods separately using the following method.  
 163 For a given model and 30-year period:

- 164 (1) We extract SSTs from each ensemble member for the 30-year period of interest.
- 165 (2) We then remove the long-term monthly mean SSTs at each grid point based on the  
166 contemporaneous climatology calculated using all ensemble members (i.e., anomalies  
167 in 1921-1950 are relative to a 1921-1950 climatology).
- 168 (3) We further remove the ensemble mean SST anomaly (SSTA) (i.e., the model-specific  
169 externally-forced signal) at each grid point from each of the model's individual  
170 ensemble members.
- 171 (4) We arbitrarily treat the 1<sup>st</sup> ensemble member as the "truth" or "observations". Because  
172 each ensemble member is independent from one another, a data library of possible  
173 analog matches to the "observations" can then be constructed for each month using the  
174 remaining ensemble members. For example, the data library for January in CESM1-LE  
175 consists of 39 ensemble members x 28 years = 1092 samples. Note that it is only 28  
176 years because we aim to generate 24-month forecasts, so any possible analog matches  
177 in the final two years would extend beyond our 30-year window of interest. Thus, the  
178 final two years in each 30-year window are excluded from our data libraries.
- 179 (5) For a given time step, we choose analogs by minimizing the distance between the  
180 climate state in the "observed" ensemble member and those found in the corresponding  
181 monthly data library (i.e., by comparing an "observed" January to the January data  
182 library). The distance between climate states is estimated by calculating the total root-  
183 mean-squared (RMS) difference between the "observed" SSTAs from 60°S-60°N and  
184 at all longitudes and those from every possible match in the data library. Note that we  
185 do not area weight the RMS difference calculation used in our analysis (see following  
186 section for more details). The distances are then ranked in descending order. The 10  
187 closest states from the data library and their subsequent 24-month evolution are chosen  
188 as the forecast ensemble for that time step.
- 189 (6) We repeat (1)-(5) by treating each other model ensemble member as "observations"  
190 and constructing the monthly data library using the remaining ensemble members.

191 This procedure generates a 10-member forecast for every timestep and every ensemble  
192 member in a given model LE. For example, applying this perfect model framework to CESM1-LE  
193 for a given 30-year period generates 40 (ensemble members) x 12 (months) x 28 (years) x 10  
194 (forecast members) = 134,400 24-month forecasts with which we can estimate seasonal climate

195 predictability. Although we use SSTAs to identify analogs, we are not limited only to SSTA  
196 forecasts for analysis. Once the nearest climate states are selected, the evolution of any model  
197 variable can be treated as a forecast and subsequently verified against the corresponding variable  
198 from “observations” (e.g., Ding et al., 2019). In this way, we assess the forecast anomalies of the  
199 following variables from each model, with the CMIP standard variable name shown in parenthesis:  
200 SST (tos), 2m temperature over land (tas), precipitation (pr), and the 500mb streamfunction, which  
201 was calculated using the U/V wind components at 500mb (ua, va). As previously mentioned for  
202 SST, anomalies for all other variables are derived by removing both the long-term monthly means  
203 of the contemporaneous 30-year period and each model’s respective ensemble mean.

204

205 *(c) Perfect model-analog sensitivities*

206         There are several arbitrary choices that must be made when adapting the perfect model-  
207 analog technique for LEs. Here, we briefly discuss these decisions and how they might influence  
208 our results or conclusions. (1) We remove a given model’s ensemble mean from each of its  
209 members in order to isolate the internal component of each parameter, while still allowing for the  
210 rectification of the forced response on climate variability. Doing so allows us to focus on possible  
211 forced changes in the predictability of climate variations, as opposed to the more trivial exercise  
212 of predicting the forced trend. (2) Ding et al. (2018) showed that for data libraries of several  
213 hundreds of years, analog forecast ensembles of 10-20 members produced the most accurate  
214 forecasts. This is because larger forecast ensembles include increasingly poor analog matches,  
215 resulting in lower skill over the length of the forecast. We choose the top 10 analogs for our  
216 forecast ensembles for computational efficiency; however, our results and conclusions are not  
217 qualitatively impacted when increasing the forecast ensemble size to the top 15 or 20 matches. (3)  
218 We do not area weight the RMS difference calculation so as not to overweight the tropics when  
219 drawing analogs. We find that this choice increases the overall forecast skill in the mid-latitudes  
220 without overly decreasing it in the tropics. We select analogs based on SSTAs from 60°S-60°N  
221 and at all longitudes for similar reasons (i.e., to improve the representation of the extratropics when  
222 selecting analogs). Our results and conclusions are not qualitatively impacted by these decisions.

223

224 *(d) Potential predictability metrics and signal-to-noise*



225 To assess lead-dependent potential skill in each model, we calculate  $N_e$  estimates of the  
226 anomaly correlation coefficient (ACC) between each ensemble mean forecast and the  
227 corresponding “observations”, where  $N_e$  is the number of ensemble members in a given LE (i.e.,  
228 the number of “observed” timeseries used to generate analogs). For example, there are 40 estimates  
229 of the ACC for 1921-1950 when evaluating CESM1-LE. We repeat this procedure for each 30-  
230 year period separately, and we report the ensemble mean ACC in our results. We test the  
231 significance of the ensemble mean ACC using a 95% confidence interval based on two-sample  $t$ -  
232 test. We further determine the robustness of the change in ACC between 30-year periods by  
233 indicating where 80% of a given model’s ensemble members agree on the sign of the change.

234 We further evaluate the forecasts using the reliability categories proposed by Weisheimer  
235 & Palmer (2014). Reliability categories are advantageous because they provide a highly  
236 interpretable measure of whether a forecast system is useful for decision making. Overall, there  
237 are five categories. Forecasts that fall into reliability category 5 are considered “Perfect”, category  
238 4 = “Very Useful”, category 3 = “Marginally Useful”, category 2 = “Not Useful”, and category 1  
239 = “Dangerously Useless”. Reliability categories are defined by the slope of a forecast system’s  
240 reliability diagram, which simply plots the observed frequency of a given event (say temperatures  
241 in the upper tercile) for different forecast probability bins. The slope of the reliability diagram is  
242 estimated using a weighted linear regression, where the weights are the number of samples in each  
243 probability bin. Using a bootstrapping technique with replacement, the uncertainty around the  
244 reliability slope is estimated by randomly resampling the forecasts and recomputing the slope. The  
245 reliability category is then determined based on the sign and magnitude of the reliability slope and  
246 whether or not the uncertainty intervals encompass the one-to-one perfect reliability line. See  
247 Weisheimer & Palmer (2014) for more details.

248 In our analysis, we assess the reliability categories of surface temperature and precipitation  
249 in the upper and lower terciles. We follow Weisheimer & Palmer (2014) with the following  
250 exceptions. First, for computational efficiency, we resample our forecasts 500 times when applying  
251 the bootstrapping algorithm. Second, we include the full range of reliability slope uncertainty (i.e.,  
252 a 100% confidence interval) when calculating categories. Finally, because we are able to draw a  
253 large number of forecasts from the LEs ( $>100,000$ ), we have enough data to calculate reliability  
254 categories at each grid cell. However, for brevity, we only show the fraction of the global area that  
255 falls within each category in our results. This contrasts from Weisheimer & Palmer (2014) and

256 others who, in order to achieve a larger sample size, calculated a single reliability metric for large  
257 areas (e.g., all of North America) by aggregating short hindcast records in space. We do not expect  
258 any of these methodological differences to qualitatively influence our results or conclusions.

259 Finally, we assess the lead-dependent signal-to-noise (S2N) ratio in our forecasts following  
260 Sardeshmukh et al. (2000). For each model ensemble member  $e$ , the S2N ratio at lead  $l$  is:

$$261 \quad S2N(e, l) = \left( \frac{\sum_{i=1}^n \bar{x}_f^2}{\frac{1}{K} \sum_{i=1}^m x_f'^2} \right)^{1/2} \quad (1)$$

262 Where  $x_f' = x_f - \bar{x}_f$  is the deviation of each individual forecast member ( $x_f$ ) from the ensemble  
263 mean forecast ( $\bar{x}_f$ ) at each time step  $n$ , and  $m$  is  $n$  times the number of forecast ensemble members  
264  $K$  (in our analysis  $K = 10$ ). Therefore, for a given 30-year period,  $n = 12$  (months)  $\times$  28 (years) =  
265 336 and  $m = 3360$ . As with ACC, we calculate  $N_e$  estimates of the S2N ratio for each LE (one for  
266 each ensemble member), and report the ensemble mean values in our results. A higher S2N ratio  
267 indicates that there is a larger ensemble mean anomaly and/or less spread among the forecast  
268 ensemble, which results in a more skillful forecast in the perfect model framework (Sardeshmukh  
269 et al. 2000).

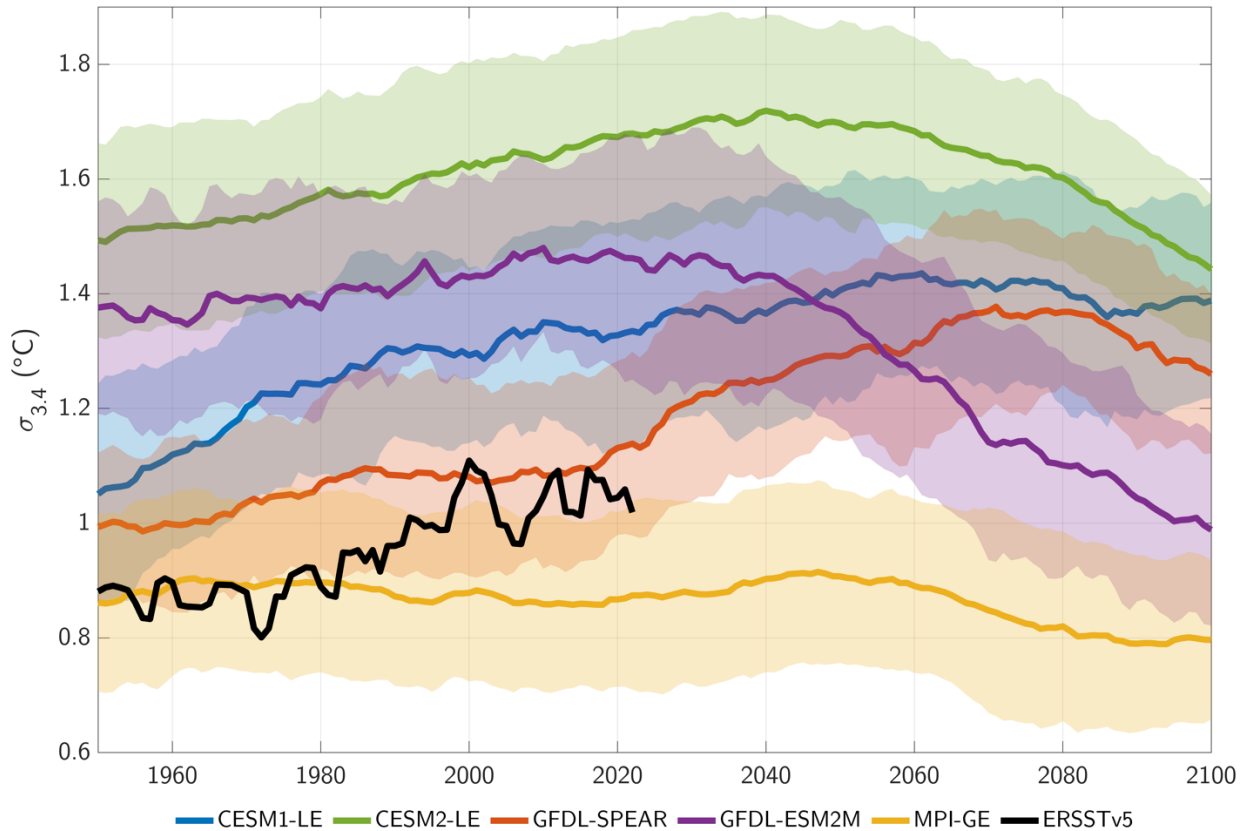
270

### 271 **3. Results**

#### 272 *(a) Forced changes in ENSO amplitude*

273 Given ENSO's dominant role in driving seasonal climate predictability, we first assess the  
274 simulated response of ENSO amplitude to historical and future radiative forcing in each LE. The  
275 CESM1-LE shows a consistent increase in Nino3.4 (i.e., SST anomalies or SSTA, averaged 5°S-  
276 5°N, 170°W-120°W) standard deviation from 1921-2060, after which it levels off (Figure 1 and  
277 Table 1). The Nino3.4 amplitude in GFDL-SPEAR is relatively stable from 1921-2020, after  
278 which it increases until about 2080 before decreasing slightly. In contrast, the ENSO variability in  
279 CESM2-LE rises consistently through 2040 before decreasing consistently through 2100. The  
280 positive ENSO amplitude trends from 1921-2022 in the ensemble means of CESM1-LE, CESM2-  
281 LE and GFDL-SPEAR compare favorably to observations (Figure 1 black line; Table 1), although  
282 CESM1-LE and CESM2-LE show large positive ENSO variability biases. While GFDL-ESM2M  
283 also exhibits positive ENSO variability biases, its Nino3.4 standard deviation is relatively stable  
284 until about 2040, after which it sharply decreases through the end of the century. In MPI-GE, there  
285 is little change in Nino3.4 variability throughout the record. The large inter-model uncertainty in

286 future ENSO variability is consistent with Maher et al. (2023) (see their Figure 4). Based on these  
 287 results, we primarily focus on CESM1-LE, MPI-GE, and GFDL-ESM2M when evaluating the  
 288 forecast skill of our perfect model-analogs as these LEs span the range of possible changes in  
 289 future ENSO amplitude (i.e., increasing, no change, and decreasing, respectively).  
 290



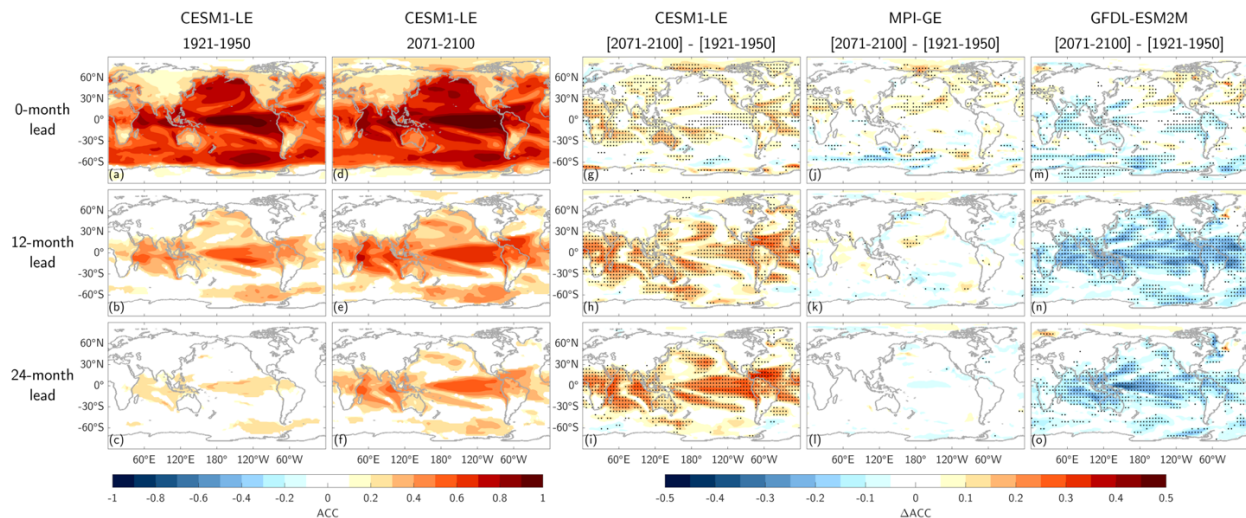
291  
 292 **Figure 1** Standard deviation of December-February averaged SSTA in the Nino3.4 region in running 30-year  
 293 windows from 1921-2100. Years indicate end of the window (e.g., 1960=1931-1960). Colors represent different  
 294 model large ensembles, with thick curves for ensemble mean values and shading for the one standard deviation  
 295 spread across the ensemble. Black curve shows the observed values based on ERSSTv5 from 1921-2022.  
 296

297 (b) Potential predictability and future changes, ACC

298 **1) Sea surface temperature and surface air temperature**

299 Perfect model-analog forecasts (hereafter referred to as “forecasts”) of SSTA for 1921-  
 300 1950 in CESM1-LE show significant potential skill (hereafter referred to as “skill”) at 0-month  
 301 lead for most of the globe (globally averaged ACC = 0.62), with the tropical Pacific exhibiting the  
 302 highest skill (ACCs > 0.9; Figure 2a). There is also significant skill of surface air temperature  
 303 anomalies over land (SATA) at 0-month lead in most regions. However, SATA skill is generally

304 weaker than for SSTA (global average ACC = 0.48), especially in mid-latitudes. The higher overall  
 305 SSTA skill or “potential predictability” (hereafter referred to as “predictability”) at 0-month lead  
 306 is expected since our analogs are chosen by minimizing the distance between the “observed” SSTA  
 307 and the data library. Indeed, the high 0-month lead SSTA skill gives us confidence that the perfect  
 308 model framework is reliably drawing analogs that closely correspond to the “observed” climate  
 309 states at each time step. Results are similar for the other LEs (Figures S1-S5).  
 310



311  
 312 **Figure 2** Surface temperature potential predictability. (a)-(c) Ensemble mean skill of surface temperature  
 313 anomalies in CESM1-LE as measured by ACC calculated across all months in the period 1921-1950. (d)-(f) As  
 314 in (a)-(c), but for the period 2071-2100. (g)-(o) Change in ACC between past and future periods for (g)-(i)  
 315 CESM1-LE (j)-(l) MPI-GE (m)-(o) GFDL-ESM2M. Skill values in (a)-(f) are only shown when 95% significant.  
 316 Stipples in (g)-(o) indicate where 80% of a respective model’s ensemble agrees on the sign of the change. See  
 317 Figures S1-S5 for the full surface temperature anomaly skill in the other large ensembles.  
 318

319 We further assess the predictability at increasing lead times; however, for brevity, we only  
 320 show the skill at 12-month and 24-month leads (Figure 2b-c; see Figures S1-S5 for skill maps at  
 321 additional lead times). Skill of surface temperature decreases with increasing lead time, although  
 322 this reduction is more apparent for SATA than for SSTA. This difference is consistent with the  
 323 higher thermal capacity of the ocean relative to the atmosphere, which typically leads to higher  
 324 predictability at longer leads for SSTA than for SATA. In particular, SSTA ACCs at 12-month  
 325 lead exceed 0.6 in the tropical Pacific, consistent with previous model-analog forecast studies (e.g.,  
 326 Ding et al., 2018). There is also significant SATA predictability over tropical land surfaces, as well  
 327 as significant SSTA predictability throughout most of the North Pacific, the tropical Atlantic, the  
 328 tropical Indian Ocean, and the Southern Ocean west of the Drake Passage. These regions are

329 known to be influenced by large-scale ENSO teleconnections (e.g., He et al., 2020; Horel &  
330 Wallace, 1981; Mo & Ghil, 1987), suggesting that ENSO is a key source of long-lead predictability  
331 in our forecasts. Skill further degrades out to 24-month leads (Figure 2c); however, there is still  
332 the significant SATA skill over northern South America and significant SSTA skill in the tropical  
333 and South Pacific and the Indian Ocean.

334 In CESM1-LE, there is a robust increase in SSTA and SATA predictability in the future at  
335 all leads, with only a few small regions of decreasing predictability (Figures 2d-i). In particular,  
336 the 0-month lead SSTA skill increases in the western tropical Pacific as well as the Indian and  
337 Atlantic Oceans (Figure 2i). Similarly, there is a robust increase in future SATA predictability at  
338 0-month lead over much of Africa, portions of eastern Asia, equatorial South America, and all of  
339 Australia. An increase in forecast skill at 0-month lead implies that the distance between the  
340 “observed” and analog climate states decreases in the future (i.e., the analogs more closely match  
341 the “observations”). Further, the widespread ensemble agreement (black stipples) indicates that  
342 these predictability changes are a “robust” (defined here as 80% ensemble agreement on the sign  
343 of the change) part of the model’s forced response and not due to random natural decadal  
344 variations.

345 The CESM1-LE changes in SSTA/SATA predictability are starker at 12 and 24-month leads  
346 (Figures 2h-i), with robust increases in ACC throughout the global tropics in an ENSO-like pattern.  
347 The increased predictability along the equatorial Pacific, in particular, suggests that ENSO itself  
348 is more predictable in the future in CESM1-LE. We will explore ENSO predictability in more  
349 detail in Section 3d. There are also robust long-lead increases in SSTA and SATA predictability  
350 in the mid-latitudes. For example, there is an increase in SSTA skill in the North Atlantic in a  
351 pattern reminiscent of the SSTA footprint generated by the NAO (i.e., a horseshoe shape from  
352 southern Greenland to the tropical North Atlantic; Kushnir et al., 2006). There are also pronounced  
353 increases in SSTA skill in the North Pacific and along the U.S. west coast and SATA skill in the  
354 American Southwest, which may be associated with an eastward shift in ENSO’s teleconnections  
355 to the Pacific North America region (O’Brien and Deser 2023). Other LEs generally disagree with  
356 CESM1-LE on the sign and magnitude of future predictability changes (Figure 2j-o and Figures  
357 S1-15). The MPI-GE at 0-month lead shows some isolated regions of increasing and decreasing  
358 SSTA/SATA skill, but without a clear pattern. At longer leads, the skill change in MPI-GE is close  
359 to zero nearly everywhere and there is little agreement among the ensemble on the sign of the

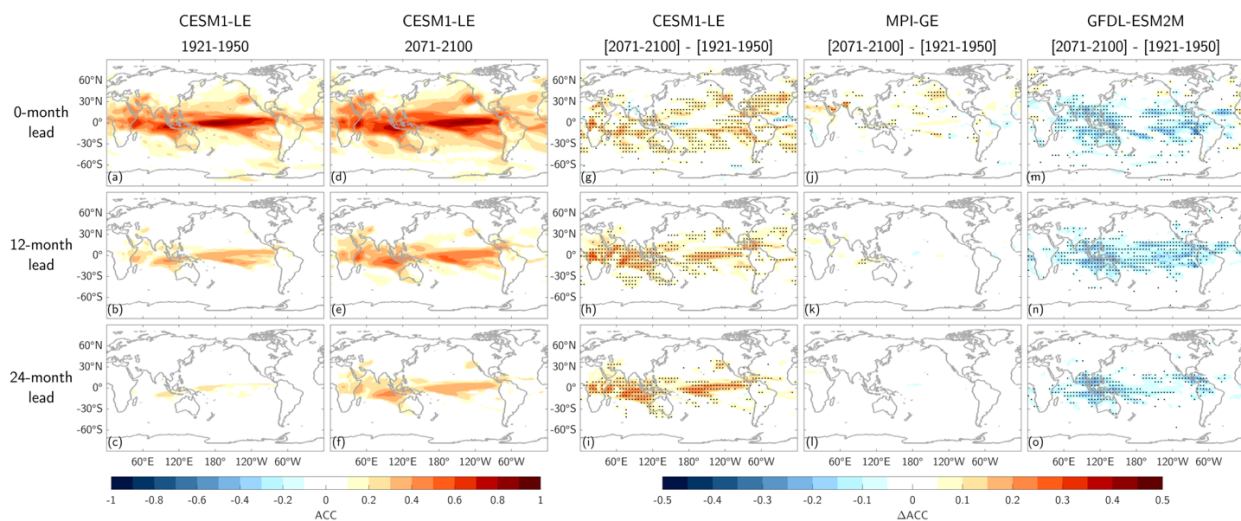
360 change. In contrast, GFDL-ESM2M shows a robust decrease in SSTA/SATA predictability for  
 361 most the globe (Figure 2m-o) in a similar ENSO-like pattern as seen in CESM1-LE (pattern  
 362 correlation = -0.68 at 12-month lead), though with less loading in the Northeast Atlantic. This  
 363 suggests that ENSO predictability decreases in the future in GFDL-ESM2M.

364

## 365 2) Precipitation

366 Forecasts of precipitation anomalies for 1921-1950 in CESM1-LE show peak skill over the  
 367 tropical oceans (Figure 3a-c; see Figures S6-S10 for other models). For example, 0-month lead  
 368 precipitation skill is highest over the central equatorial Pacific, with ACCs exceeding 0.9. There  
 369 is also significant skill at 0-month lead over tropical land surfaces and in the mid-latitudes along  
 370 the U.S. west coast. Precipitation predictability similarly decreases with increasing lead, with only  
 371 the equatorial Pacific and Indian Oceans displaying any significant skill at 12-month lead. By 24-  
 372 month lead, precipitation predictability is generally insignificant, except for isolated regions in the  
 373 Indo-Pacific warm pool.

374



375

376 **Figure 3** As in Figure 2, but for precipitation predictability.

377

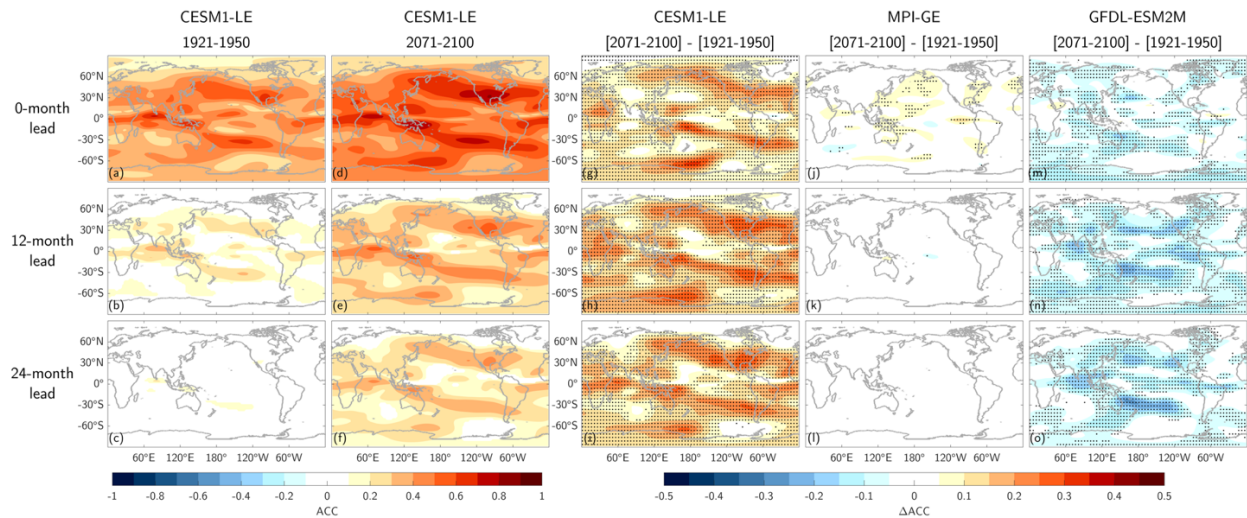
378 Similar to SSTA/SATA, there are robust increases in future precipitation predictability at  
 379 all leads in CESM1-LE (Figure 3d-i), with centers of action in the Indian Ocean, the equatorial  
 380 Pacific, the Caribbean, and the U.S. west coast. The North Atlantic also shows robust increases in  
 381 predictability at 0- and 12-month lead. The increase in predictability at 24-month lead is of particular  
 382 note given that there is virtually no significant skill in the past. In the future, however, there is

383 significant predictability over the equatorial Pacific and Indian Oceans. Additionally, the region  
 384 of highest skill along the equatorial Pacific shifts eastward from about the dateline in the period  
 385 1921-1950 to about 140°W in the period 2071-2100. This eastward shift may be related to CESM1-  
 386 LE simulated El Niño events shifting eastward in the future (O’Brien and Deser 2023; Williams  
 387 and Patricola 2018). The sign and relative magnitude of the skill changes in the other LEs are also  
 388 consistent with their respective SSTA/SATA predictability changes (Figures 3j-o). Specifically,  
 389 MPI-GE once again shows isolated regions of robust precipitation skill change at 0-month, but no  
 390 significant change at longer leads. Similarly, GFDL-ESM2M shows a robust decrease in  
 391 precipitation predictability at all leads throughout the tropics.

392

### 393 3) Upper atmosphere circulation

394 Forecasts of 500mb streamfunction anomalies ( $\psi_{500}$ ) during the period 1921-1950 in  
 395 CESM1-LE show significant skill at 0-month and 12-month leads (Figure 4a-c; see Figures S11-  
 396 S15 for other models). In particular, there are regions of high ACC in the subtropical and mid-  
 397 latitude North and South Pacific as well as over North America. These centers of action are  
 398 consistent with the locations of the PNA and Pacific-South American (PSA) patterns (Horel and  
 399 Wallace 1981; Mo and Ghil 1987). Combined, these two results suggest that the forecasts are  
 400 successfully capturing the upper atmospheric wave train response to tropical heating anomalies  
 401 associated with ENSO.



402

403 **Figure 4** As in Figure 2, but for 500mb streamfunction ( $\psi_{500}$ ) predictability.

404

405 In the future, there is a near-global increase in CESM1-LE  $\psi_{500}$  predictability at all leads  
406 (Figure 4d-i). Of note are the increases in  $\psi_{500}$  ACC in the PNA and PSA regions, respectively,  
407 which may be an indication of stronger ENSO teleconnections in CESM1-LE in the future  
408 (O'Brien and Deser 2023). The robust predictability increases in the PNA region are also  
409 consistent with the increases seen in both SSTA/SATA and precipitation predictability along the  
410 U.S. west coast (see Figures 2g-i and 3g-i). Similar to precipitation forecasts, long-lead  $\psi_{500}$   
411 predictability is especially impacted in CESM1-LE, with significant increases in predictability  
412 nearly everywhere at 24-month lead. As with SSTA, SATA, and precipitation, the other LEs  
413 disagree with CESM1-LE on the sign of future  $\psi_{500}$  predictability changes (Figure 4j-o). MPI-GE  
414 shows no regions of robust predictability changes beyond 0-month lead, and GFDL-ESM2M once  
415 again produces a decrease in  $\psi_{500}$  skill for most of the globe. In particular, GFDL-ESM2M shows  
416 a decrease in predictability in the PNA and PSA regions of the North and South Pacific, which  
417 may suggest that ENSO-related teleconnections in this model are weaker in the future.

418

419 *(c) Potential predictability and future changes, reliability*

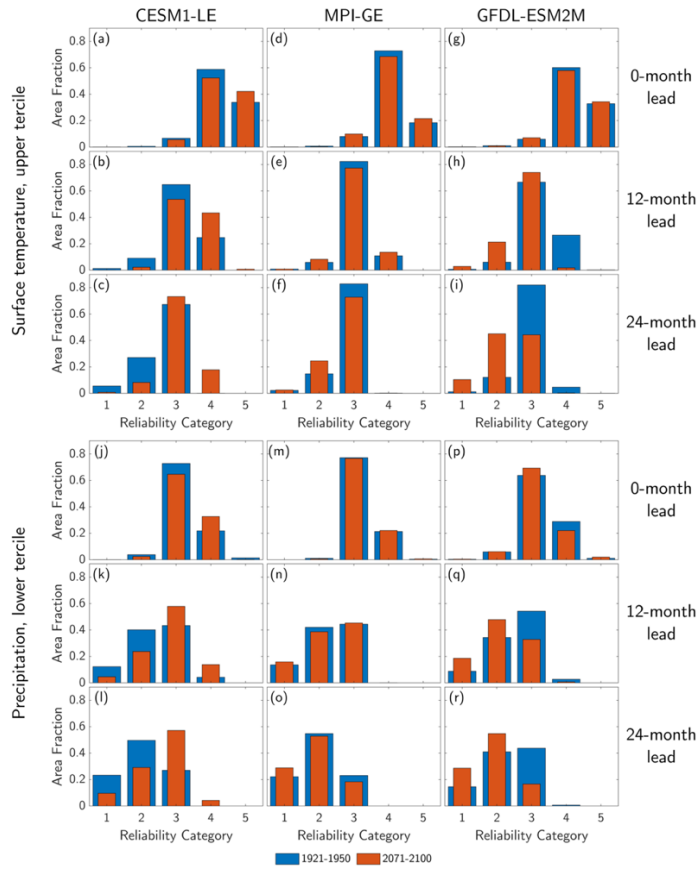
## 420 **1) Surface temperature**

421 To test the sensitivity of our results to our choice of skill metric, we further evaluate future  
422 changes in climate predictability using probabilistic reliability categories. Upper tercile surface  
423 temperature (including SSTA and SATA) forecasts in CESM1-LE show strong reliability during  
424 the period 1921-1950 (Figure 5a-c; blue bars). For example, at 0-month lead, 34% and 59% of the  
425 globe falls within the category 5 (“perfect”) and 4 (“very useful”) forecast bins, respectively. The  
426 fraction of the globe in these higher categories decreases with increasing lead time, with the  
427 majority of forecasts across the globe falling into reliability category 3 (“marginally useful”) by  
428 12- (area fraction = 65%) and 24-month (area fraction = 67%) lead. In the future, CESM1-LE  
429 surface temperature forecasts become more reliable (Figure 5a-c; red bars), with a clear shift in  
430 the distribution towards higher reliability categories at all leads. For example, at 12-month leads,  
431 the global area fraction of forecasts that fall into reliability category 4 increases from 25% in 1921-  
432 1950 to 43% by 2071-2100, with a corresponding decrease in reliability category 2 (“not useful”)  
433 and 1 (“dangerously useless”) forecasts.

434

435





436

437 **Figure 5** Fraction of global area in each reliability category for (a)-(i) forecasts of upper tercile surface  
 438 temperature anomalies and (j)-(r) forecasts of lower tercile precipitation anomalies. Values are for 0-, 12-, and  
 439 24-month leads in (left column) CESM1-LE, (middle column) MPI-GE, and (right column) GFDL-ESM2M.  
 440 The reliability categories are 5 = perfect, 4 = very useful, 3 = marginally useful, 2 = not useful, and 1 =  
 441 dangerously useless. Each category is calculated across all months in the periods (blue) 1921-1950 and (red)  
 442 2071-2100.

443

444

445

446

447

448

449

450

451

452

453

454

For the period 1921-1950, upper tercile surface temperature forecasts from MPI-GE and GFDL-ESM2M produce a similar distribution of reliability categories as CESM1-LE (Figure 5d-i; blue bars). Both LEs have mostly category 4 and 5 forecasts at 0-month lead, with the distribution shifting towards lower reliabilities at longer leads. By 12-month lead, forecasts for 82% of the global area fall within category 3 for MPI-GE, while forecasts for 67% of the global area fall within the same category for GFDL-ESM2M. In the future period, the global area fraction within each reliability category for MPI-GE remains relatively stable at all leads (Figure 5d-f), with only a small decrease in category 3 forecasts (from 83% to 73%) and corresponding increase in category 2 forecasts at 24-month lead (from 15% to 25%). While the reliability distribution for GFDL-ESM2M forecasts do not change much at 0-month, there is a noticeable shift towards lower categories at 12- and 24-month lead going from the period 1921-1950 to 2071-2100 (Figure 5h-i).

455 At 24-month lead, the global area fraction with category 3 forecasts in GFDL-ESM2M decreases  
456 from 82% to 44% and the global area fraction with category 2 forecasts increases from 12% to  
457 45%. Therefore, forecasts of upper tercile surface temperature in GFDL-ESM2M become less  
458 reliable in the future for most of the globe, consistent with the decreasing ACCs shown previously.

459

## 460 **2) Precipitation**

461 Repeating this analysis for lower tercile precipitation forecasts, we find that the CESM1-  
462 LE precipitation forecasts are overall less reliable than the surface temperature forecasts, as  
463 indicated by skew of the reliability distribution towards category 1-3 forecasts at all leads (Figure  
464 5j-l). However, the future change in lower tercile precipitation forecast reliability in CESM1-LE  
465 is consistent with that seen in upper tercile surface temperature, with a clear shift in the distribution  
466 towards higher categories. For example, at 24-month lead, the global area fraction with category  
467 3 forecasts increases from 27% to 57% between 1921-1950 and 2071-2100 with a corresponding  
468 decrease from 50% to 29% for category 2 forecasts. The future changes in lower tercile  
469 precipitation reliability in MPI-GE and GFDL-ESM2M are also consistent with their respective  
470 surface temperature reliability changes, with MPI-GE forecasts showing little change in the  
471 reliability distribution (Figure 5m-o), and GFDL-ESM2M showing a clear shift towards categories  
472 1-2 (Figure 5p-r). In particular, at 24-month lead in GFDL-ESM2M, the area fraction with category  
473 3 forecasts decreases in the future from 44% to 17%, with a corresponding increase in category 1  
474 and 2 forecasts. The above results are consistent for lower and upper tercile forecasts of surface  
475 temperature and precipitation, respectively (Figure S16).

476

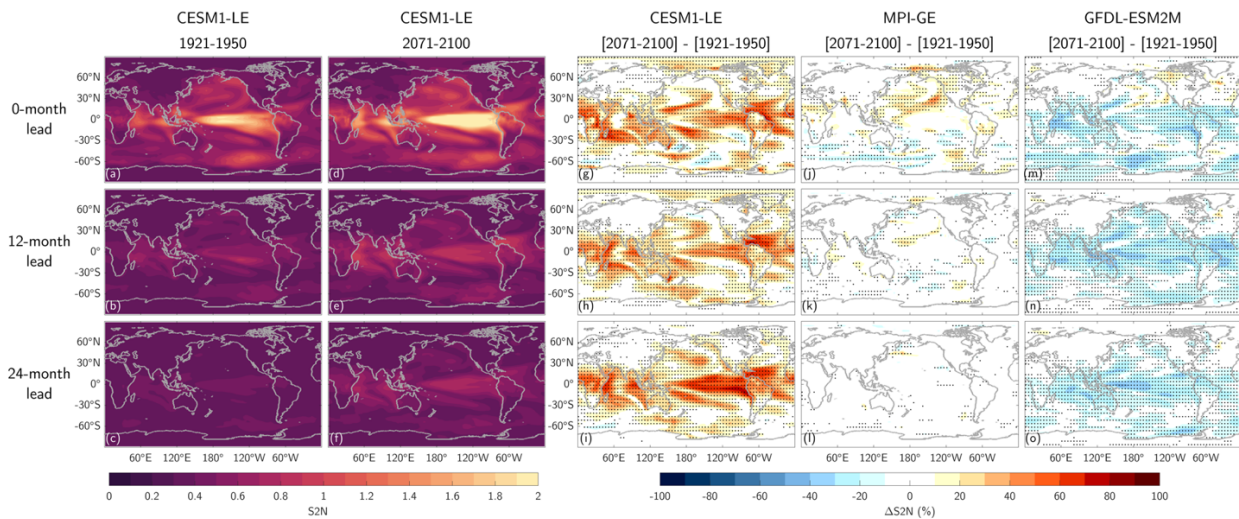
477 *(d) Linking future predictability changes and ENSO amplitude*

### 478 **1) Signal-to-Noise**

479 To briefly summarize the above results, seasonal climate predictability in the future  
480 generally increases in CESM1-LE, does not change in MPI-GE, and decreases in GFDL-ESM2M,  
481 as measured by different forecast skill metrics (ACC and reliability) across multiple variables  
482 (SSTA, SATA, precipitation, and  $\psi_{500}$ ). While the models disagree on the sign of future  
483 predictability changes, they are each self-consistent with their projected change in future ENSO  
484 amplitude (i.e., Figure 1). The link between future climate predictability and future ENSO  
485 amplitude may be related to ENSO's role as the dominant internal climate mode, allowing one to

486 detect its influence across much of the globe despite the presence of other forms of variability (e.g.,  
 487 weather or other climate modes). For example, if ENSO amplitude increases in the future (e.g., as  
 488 projected by CESM1-LE), then that may lead to an increase in the signal-to-noise (S2N) ratio of  
 489 ENSO and its teleconnections, which would tend to contribute to an overall more deterministic  
 490 climate system and more skillful forecasts (e.g., Sardeshmukh et al., 2000). To test this hypothesis,  
 491 we calculate changes in the S2N ratio (Eq. 1) for surface temperature as a function of lead time in  
 492 each of the two time periods (Figure 6). During the period 1921-1950, the S2N ratios in CESM1-  
 493 LE forecasts at 0-month lead follow an ENSO-like pattern, with the highest values in the equatorial  
 494 Pacific (maximum value = 1.94). Weaker (but still elevated) values are seen in the Indian Ocean,  
 495 the South Pacific, the Northeast Pacific along the U.S. west coast, the North Atlantic, and over the  
 496 tropical African and South American land surfaces (Figure 6a). The S2N decreases with increasing  
 497 lead time (Figure 6b-c); however, the ENSO-like pattern of elevated S2N persists at 12-month lead  
 498 before mostly dissipating at 24-month lead.

499



500

501 **Figure 6** Signal-to-noise (S2N) ratios for surface temperature anomaly forecasts. (a)-(c) Ensemble mean S2N  
 502 of surface temperature forecasts in CESM1-LE calculated across all months in the period 1921-1950. (d)-(f) As  
 503 in (a)-(c), but for the period 2071-2100. (g)-(o) Percent change in S2N between past and future periods for (g)-  
 504 (i) CESM1-LE (j)-(l) MPI-GE (m)-(o) GFDL-ESM2M. Stipples in (g)-(o) indicate where 80% of a respective  
 505 model's ensemble agrees on the sign of the change.

506

507 The patterns of future S2N change in each of the LEs are remarkably similar to the surface  
 508 temperature ACC changes seen in Figure 2 (Figure 6d-o), with pattern correlations between the  
 509 ACC and S2N maps at 0-, 12-, and 24-month lead of 0.86, 0.97, and 0.98 for CESM1-LE, 0.76,  
 510 0.90, and 0.83 for MPI-GE, and 0.69, 0.95, and 0.95 for GFDL-ESM2M, respectively.

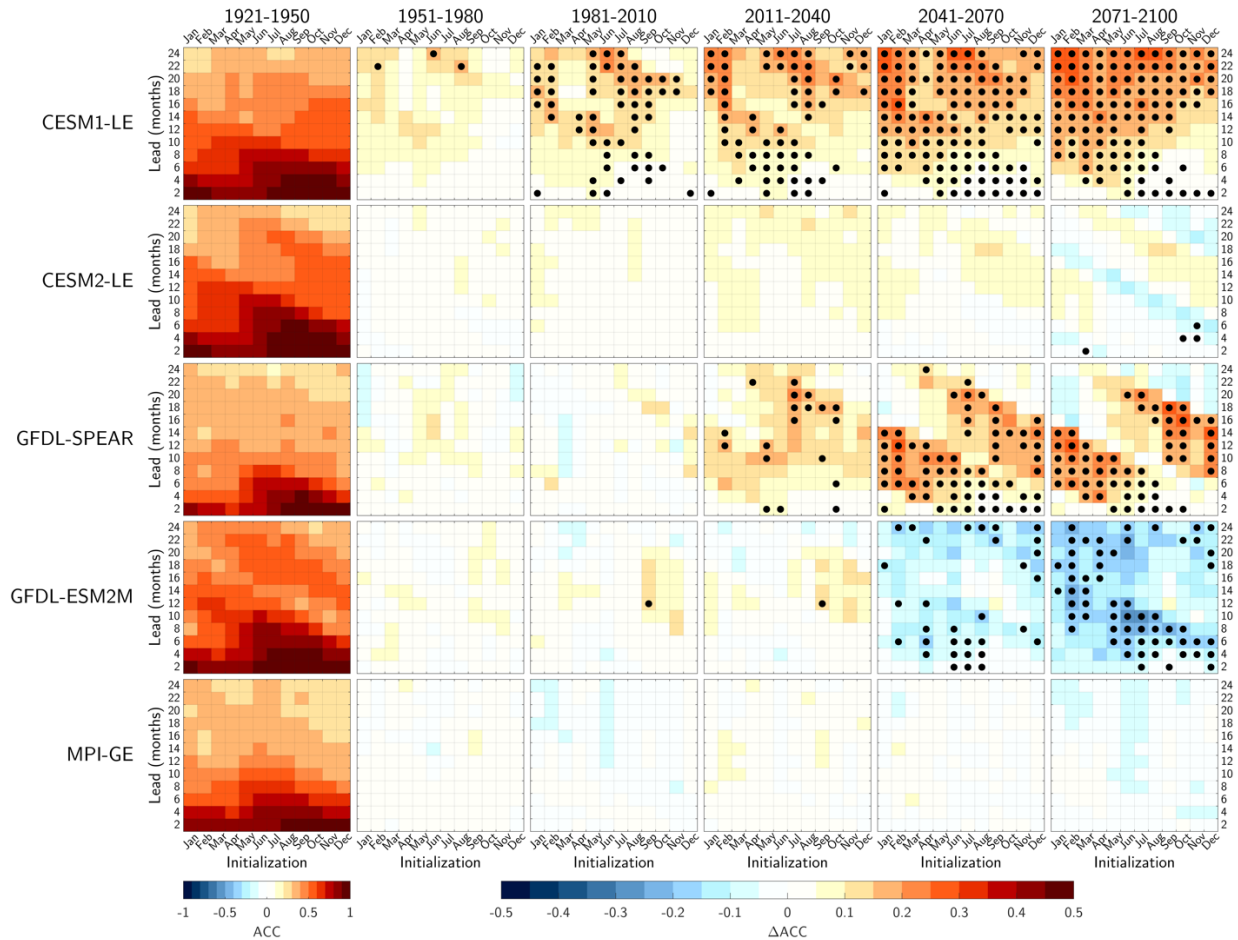
511 Decomposing the S2N equation into a signal and noise component (i.e., the numerator and  
512 denominator of Eq. 1, respectively), we find that the changes in the signal are over five times larger  
513 than changes in the noise for much of the globe (Figures S17-S18). For example, the signal change  
514 averaged 60°S-60°N at 12-month lead in CESM1-LE is 27%, compared to just a 4.7% change in  
515 the noise. In the case of CESM1-LE, this indicates that the amplitude of a typical ensemble mean  
516 forecast anomaly is larger in the future without a substantial increase in the average forecast spread  
517 (i.e., the forecast uncertainty). These results are consistent with previous studies linking ENSO  
518 amplitude to S2N and/or climate predictability (Capotondi et al., 2015; Chen et al., 2004; Gu &  
519 Philander, 1997; Sardeshmukh et al., 2000; Suarez & Schopf, 1988; Weisheimer et al., 2022; Zhao  
520 et al., 2016).

521

## 522 **2) Time-varying potential predictability changes, Nino3.4**

523 To further relate changes in ENSO amplitude to global predictability, we explore skill  
524 changes as a function of time. A time-varying perspective of predictability is important given the  
525 non-monotonic changes in ENSO amplitude seen in most LEs (e.g., Figure 1). Such variability in  
526 each model's forced ENSO response may give rise to periods of predictability that differ not only  
527 from the historical period, but also from the total changes seen at the end of the 21<sup>st</sup> century (i.e.,  
528 Figures 2-4). Further, by evaluating whether time-varying skill changes are robust across a given  
529 model's ensemble, we can quantitatively estimate the "time of emergence" for forced changes in  
530 predictability within each model.

531 To illustrate, we show the forecast skill of SSTAs averaged in the Nino3.4 region for six  
532 different 30-year periods from 1921-2100 (Figure 7). In addition to CESM1-LE, MPI-GE, and  
533 GFDL-ESM2M, we also include CESM2-LE and GFDL-SPEAR in this analysis as ENSO  
534 amplitude changes in these models are particularly varied, with prolonged periods of increasing  
535 and decreasing variability. Treating 1921-1950 as the base period, Nino3.4 skill tends to be highest  
536 (exceeding 0.8) at leads of less than ~6 months and for forecasts initialized in boreal fall and winter  
537 (Figure 7; left column). For boreal spring and summer initializations, predictability tends to be  
538 similarly elevated at leads that encompass boreal winter in the forecast. For example, June  
539 initialized forecasts in GFDL-ESM2M show a peak in Nino3.4 skill at 2-10 month leads, and then  
540 again at 16-22 month leads (i.e., October-April of the following year).



541

542 **Figure 7** First column: Ensemble mean Nino3.4 potential forecast skill (ACC) as a function of initialization  
 543 month (x-axis) and lead time (y-axis) for each model large ensemble. Second-fifth columns: Difference in  
 544 Nino3.4 skill between the base period 1921-1950 and different 30-year periods. For example, the second column  
 545 shows the difference in skill between the periods 1951-1980 and 1921-1950. Stipples indicate that 80% of the  
 546 respective model ensemble agrees on the sign of the change.

547

548 There is little change in Nino3.4 skill in any of the models for the adjacent 30-year period  
 549 (1951-1980). However, by the period 1981-2010, CESM1-LE shows a robust increase in Nino3.4  
 550 predictability at short leads for May-September initializations and at longer leads for much of the  
 551 year. This suggests that forced changes in CESM1-LE ENSO predictability begin to emerge above  
 552 the internal noise inherent to each ensemble member during this period. In 2011-2040, CESM1-  
 553 LE Nino3.4 skill continues to increase, while GFDL-SPEAR begins to show some robust increases  
 554 in predictability. Forecast skill in CESM2 also increases slightly during this period, but there is  
 555 not widespread agreement among its ensemble on the sign of this change. We see the largest  
 556 period-to-period changes in Nino3.4 skill between 2011-2040 and 2041-2070 (Figure 7; fifth  
 557 column). For example, CESM1-LE shows robust increases in predictability for leads less than 8

558 months when initialized in boreal summer to winter and at nearly all initializations beyond 16-  
559 month lead. Forced changes to ENSO forecast skill in GFDL-SPEAR also fully emerge during this  
560 period, with diagonal bands of increased predictability associated with forecasts that verify in  
561 boreal summer to winter. In GFDL-ESM2M, robust decreases in predictability begin to emerge,  
562 but without a clear pattern. Finally, by the period 2071-2100, CESM1-LE and GFDL-SPEAR  
563 largely maintain the increases in ENSO predictability observed in the previous epoch, while forced  
564 decreases in Nino3.4 forecast skill are now fully evident in GFDL-ESM2M.

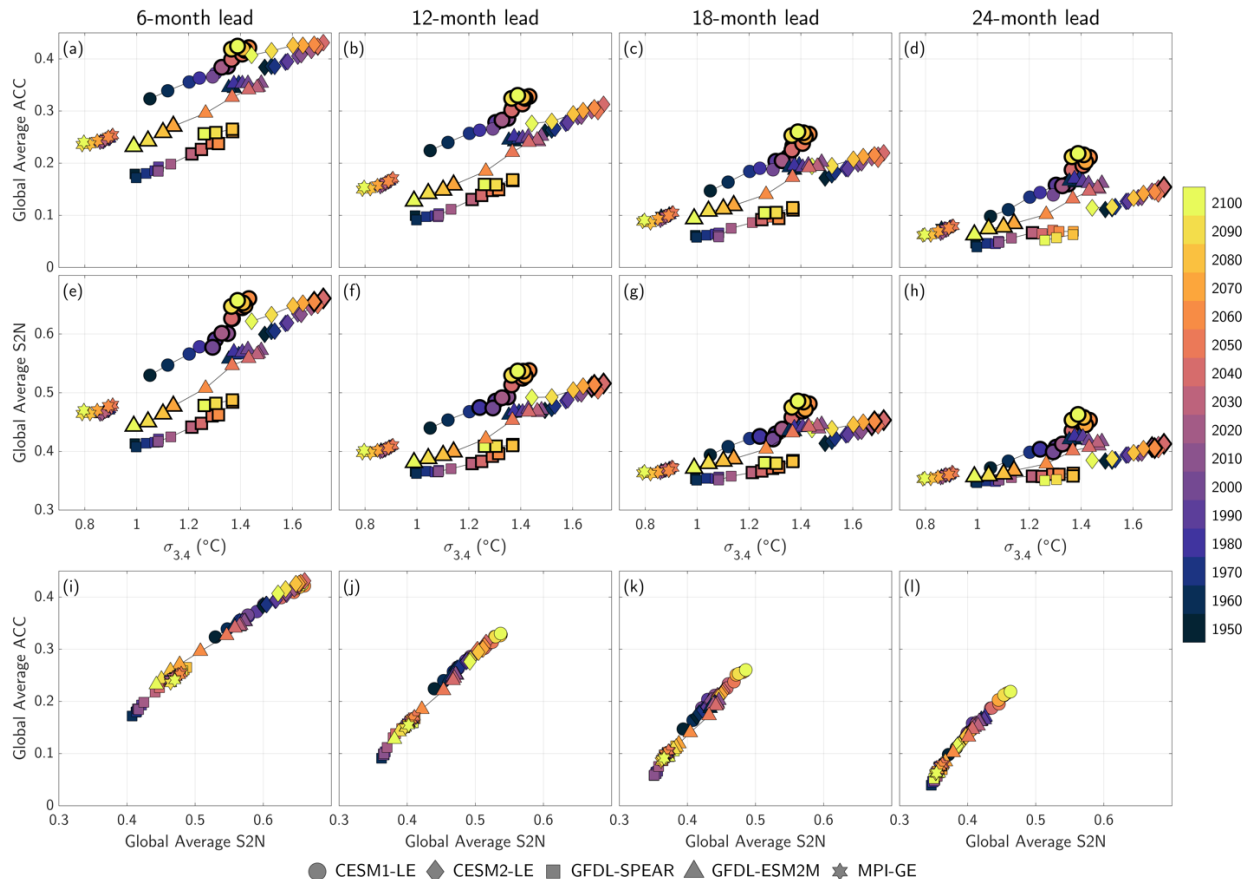
565

### 566 **3) Time-varying potential predictability changes, global**

567 There is clear model diversity in the simulated change of ENSO predictability, both in the  
568 sign and intensity of end-of-21<sup>st</sup> century changes and in the apparent time of emergence for each  
569 model's forced response (i.e., Figure 7 black dots). However, similar to our previous results (e.g.,  
570 Figures 2-5), the sign and timing of ENSO predictability changes in each of the LEs is consistent  
571 with their respective time-varying ENSO amplitudes (Figure 1). For example, there are no robust  
572 changes in Nino3.4 forecast skill in GFDL-SPEAR until the period 2011-2040, which closely  
573 corresponds to the timing of the strongest increasing trend in this model's ENSO amplitude  
574 (comparing third row of Figure 7 to orange line in Figure 1). Similarly, ENSO predictability in  
575 GFDL-ESM2M remains relatively stable until the period 2041-2070, at which point both the  
576 forecast skill and GFDL-ESM2M's ENSO amplitude start to sharply decrease (comparing fourth  
577 row of Figure 7 to purple line in Figure 1). The ensemble mean Nino3.4 skill in CESM2-LE also  
578 shows hints of a close link to its time-varying ENSO amplitude, with a slight increase in  
579 skill/amplitude through 2040 followed by a decrease through the end of the century, though these  
580 predictability changes are not robust across the CESM2 ensemble.

581 The relationship between time-varying ENSO amplitude and climate predictability extends  
582 beyond the Nino3.4 region, manifesting on global scales via ENSO-driven changes in the S2N  
583 ratio (as previously suggested in Figure 6). Indeed, we find a high correspondence in each LE  
584 between their respective time-evolving Nino3.4 amplitude, globally averaged ACC, and globally  
585 averaged S2N ratio (Figure 8). For example, at 6-month lead, the globally averaged SSTA skill in  
586 CESM1-LE increases roughly linearly over time with increasing ENSO amplitude (Figure 8a  
587 circles;  $R = 0.95$ ; Table 2), with over 80% of the model ensemble agreeing on the sign of both the  
588 ENSO amplitude and global predictability changes beginning in the period 1981-2010 (i.e., circles

589 with thick black outline). A similar linear relationship is seen in other LEs with different ENSO  
 590 amplitude trends. For example, in GFDL-ESM2M, there is a decrease in skill over time that closely  
 591 corresponds to this model's decrease in ENSO amplitude (Figure 8a triangles;  $R = 0.97$ ), although  
 592 its forced changes in predictability are not apparent until the period 2041-2070.  
 593



594  
 595 **Figure 8** (a)-(d) Global average ensemble mean potential skill at different leads (y-axis) versus  
 596 December-February averaged Nino3.4 standard deviation (x-axis) in different 30-year periods. (e)-  
 597 (h) As in (a)-(d), but for global average forecast S2N ratio versus Nino3.4 standard deviation. (i)-  
 598 (l) As in (a)-(d), but for global average ACC versus global average S2N ratio. All ACC and S2N  
 599 values are based on ensemble mean SSTA forecasts from each model (i.e., different shapes).  
 600 Shading of each shape indicates the 30-year window over which the forecast skill, S2N ratio or  
 601 Nino3.4 standard deviation are calculated, with the year indicating the end of the window. For  
 602 example, the shading for 1950 corresponds to 1921-1950. Markers with bold outlines in (a)-(h)  
 603 indicate 30-year windows in which 80% of a given model's ensemble agree on the sign of the  
 604 change (relative to 1921-1950) for both the ACC/S2N and Nino3.4 standard deviation.  
 605

606 Globally averaged S2N is highly correlated in time with each model's projected ENSO  
 607 amplitude (Figure 8e-h and Table 2), consistent with the S2N maps discussed earlier. There is also

608 a near-perfect linear relationship between globally averaged S2N and ACC (Figure 8i-l and Table  
609 2), consistent with previous studies relating perfect model skill to S2N (Sardeshmukh et al. 2000).  
610 Combined, these results further support our hypothesis that time-varying changes in predictability  
611 are driven by same-sign changes in global S2N ratios, which in turn are driven by each respective  
612 LE's projected change in ENSO amplitude. The close link between ENSO amplitude, S2N, and  
613 forecast skill is consistent across lead times, models (different marker types in Figure 8), and  
614 variables (Figures S19-S20). However, the estimated time of emergence for each model's forced  
615 response in predictability varies widely from model-to-model, ranging from as early as 1981-2010  
616 in CESM1-LE to as late as 2041-2070 in GFDL-ESM2M at 6-month lead (Table 2).

617

<i>Dataset</i>	$R(\text{ACC}, \sigma_{3,4})$	$R(\text{S2N}, \sigma_{3,4})$	$R(\text{ACC}, \text{S2N})$	ToE (ACC, $\sigma_{3,4}$ )	ToE (S2N, $\sigma_{3,4}$ )
<b><i>CESM1-LE</i></b>	0.95	0.95	1.0	2010	1970
<b><i>CESM2-LE</i></b>	0.72	0.83	0.98	Not robust	Not robust
<b><i>GFDL-SPEAR</i></b>	0.97	0.96	1.0	2030	2030
<b><i>GFDL-ESM2M</i></b>	0.97	0.98	1.0	2070	2060
<b><i>MPI-GE</i></b>	0.85	0.58	0.90	Not robust	Not robust
<b><i>All models</i></b>	0.82	0.82	1.0		

618 **Table 2** Potential skill (ACC), signal-to-noise (S2N), and ENSO amplitude relationships at 6-month lead. First  
619 column: Correlation between globally averaged SSTA potential skill and December-February averaged Nino3.4  
620 standard deviation ( $\sigma_{3,4}$ ) for different 30-year windows spanning 1921-2100 (i.e., Figure 8a). Second column:  
621 As in the first column, but for globally averaged SSTA signal-to-noise (S2N) ratios (i.e. Figure 8b). Third  
622 column: As in the first column, but for globally averaged potential skill and S2N ratios. Fourth column: Time of  
623 emergence (ToE) of a given model's forced change in globally averaged SSTA predictability and ENSO  
624 amplitude. The ToE is estimated as the first 30-year period in which 80% of a given model's ensemble agrees  
625 on the sign of both the potential skill change and Nino3.4 amplitude change. Values reported only if the model  
626 ensemble continues to agree on the sign of change through the end of record. The year indicates the end of the  
627 30-year window (e.g., 2010 = 1981-2010). Fifth column: As in the fourth column, but for globally averaged S2N  
628 ratios. Results are consistent for other leads.

629

## 630 4. Summary and Discussion

631 In this study, we investigated future changes in seasonal potential predictability across five  
632 coupled GCM LEs. Using a perfect model-analog technique, we generated hundreds of thousands  
633 of synthetic seasonal forecasts to estimate predictability changes from 1921-2100. CESM1-LE  
634 consistently showed a robust increase in predictability in the future, while predictability in GFDL-  
635 ESM2M consistently decreased (e.g., Figures 2-5). These predictability changes were largest at  
636 longer leads. In contrast, seasonal predictability in MPI-GE did not exhibit significant changes.



637 While there was large inter-model uncertainty in the sign, magnitude, and timing of future climate  
638 predictability changes, we showed that a common physical mechanism emerges that allows us to  
639 anticipate how real-world predictability may change in the coming decades. In particular, the  
640 predictability changes in each model were driven by a same-sign change in their respective ENSO  
641 amplitude. For example, forecasts from models with increasing ENSO amplitude trends (e.g.,  
642 CESM1, GFDL-SPEAR, and CESM2 until ~2040) were associated with a higher S2N ratio in the  
643 future, which led to an overall more deterministic climate system and increased potential for  
644 significant forecast skill. The higher S2N ratio resulted from a larger ensemble mean forecast  
645 anomaly (i.e., signal), owing to ENSO's role as a bigger "hammer" to the climate system. The  
646 opposite was true for models with decreasing ENSO trends (e.g., GFDL-ESM2M and CESM2  
647 after ~2040).

648 While previous studies have highlighted natural variations in climate predictability in the  
649 past (e.g., Weisheimer et al., 2020), our finding that changes to potential predictability limits are a  
650 key component of the response to increased radiative forcing has important implications for future  
651 seasonal forecasting systems. Whereas natural variations in climate predictability are random in  
652 time and include periods of both high and low predictability, our model results indicate that forced  
653 changes in climate predictability are often associated with a long-term shift towards either higher  
654 or lower predictability without a prolonged return to historical baselines. This suggests that any  
655 future deviations from historical forecast skill relationships may represent a shift in the climate  
656 system towards a new predictability regime, rather than a temporary excursion driven by internal  
657 variability. Although, non-monotonic forced changes in predictability back towards historical  
658 predictability limits are also possible (e.g., as in CESM2-LE).

659 The climate models analyzed here do not agree on the direction of future predictability  
660 changes, but the close link between skill and each model's ENSO amplitude allows us consider  
661 the future direction of predictability based on recent observations. Since 1970, the observed trend  
662 in ENSO amplitude is positive (Figure 1). Should this trend persist into the future, we might also  
663 expect seasonal forecast skill to increase alongside predictability in regions strongly influenced by  
664 ENSO and its teleconnections as these portions of the climate system become more deterministic.  
665 Of course, this assumes that perfect model predictability is a reasonable proxy for "actual" skill  
666 (e.g., skill derived from a dynamical forecast system or traditional model-analog methods), which  
667 may not always be the case (e.g., Kumar et al., 2014; Weisheimer et al., 2022). Indeed, actual skill

668 can sometimes exceed potential skill, giving rise to a signal-to-noise paradox (Scaife and Smith  
669 2018).

670 While our analysis takes an important first step towards understanding future climate  
671 predictability changes, there a number of important questions that remain. First, is there a strong  
672 seasonality to future global predictability changes? Our study focused primarily on potential skill  
673 computed across all months; however, there were some seasonal differences in ENSO  
674 predictability changes (Figure 7). For example, ENSO skill changes in GFDL-SPEAR were largest  
675 for forecasts initialized (or including) boreal spring to boreal fall (Figure 7; third row).  
676 Additionally, Maher et al. (2023) showed that ENSO amplitude changes in the LEs analyzed here  
677 are stronger in some seasons (typically boreal winter) than others (see their Figure 4). Therefore,  
678 it is possible that ENSO's impact on future predictability may be seasonally dependent. Next, what  
679 other ENSO-related factors impact future climate predictability? Many studies have shown that  
680 ENSO frequency (e.g., Berner et al., 2020), flavor (i.e., central vs eastern Pacific; Capotondi et al.,  
681 2015), and asymmetry (i.e., the duration of El Niño versus La Niña events; Maher et al., 2023)  
682 may change in the future. Changes to these characteristics may alter ENSO's influence on the rest  
683 of the climate system and thereby climate predictability. Additionally, there may be changes in the  
684 background mean state (e.g., the strength of the east-west temperature gradient in the equatorial  
685 Pacific) that impact the overall climate response to ENSO (Cai et al. 2021). While we did not find  
686 a significant relationship between predictability in our forecasts and each LE's time-varying ENSO  
687 frequency or flavor preference (not shown), we encourage future studies to investigate these  
688 mechanisms in more detail.

689 Finally, although ENSO is a dominant driver of seasonal forecast skill for much of the  
690 globe, there are likely other mechanisms that contribute to the predictability limits of different  
691 regions and variables. For example, Shi et al., (2022) showed that long-term shoaling of the mixed  
692 layer in the future may reduce the thermal inertia of the ocean, thereby decreasing ocean memory  
693 and year-to-year SST persistence, especially in the mid-latitudes. Similarly, Kumar et al., (2023)  
694 found that global warming decreases soil moisture memory over North America due to an increase  
695 in potential evapotranspiration. In both cases, the reduction in climate memory increases  
696 variability at less predictable high frequencies (e.g., weather timescales) while decreasing  
697 variability at lower frequencies (e.g., seasonal and longer), thus "whitening" the power spectrum  
698 and contributing to a decrease in persistence-related predictability. However, it is still unclear to

699 what extent these changes may be offset by dynamical drivers of predictability change related to  
700 ENSO. More research is needed to unpack the dynamic versus thermodynamic contributions to  
701 future climate predictability change.

702

### 703 **Acknowledgements**

704 We thank Friedrich Burger and Thomas Frölicher for providing us with the GFDL-ESM2M data  
705 used in this study.

706

### 707 **Data Availability Statement**

708 Large ensemble datasets are available as follows:

709 CESM1-LE: <https://www.cesm.ucar.edu/projects/community-projects/MMLEA/>

710 CESM2-LE: <https://www.cesm.ucar.edu/projects/community-projects/LENS2/>

711 GFDL-SPEAR: [https://www.gfdl.noaa.gov/spear\\_large\\_ensembles/](https://www.gfdl.noaa.gov/spear_large_ensembles/)

712 GFDL-ESM2M: Provided by Friedrich Burger and Thomas Frölicher at the University of Bern.

713 MPI-GE: <https://esgf-data.dkrz.de/projects/mpi-ge/>

714 **References**

- 715 Barnett, T. P., and R. Preisendorfer, 1987: Origins and Levels of Monthly and Seasonal Forecast  
716 Skill for United States Surface Air Temperatures Determined by Canonical Correlation  
717 Analysis. *Monthly Weather Review*, **115**, 1825–1850, [https://doi.org/10.1175/1520-](https://doi.org/10.1175/1520-0493(1987)115<1825:OALOMA>2.0.CO;2)  
718 [0493\(1987\)115<1825:OALOMA>2.0.CO;2](https://doi.org/10.1175/1520-0493(1987)115<1825:OALOMA>2.0.CO;2).
- 719 Barnston, A. G., and M. K. Tippett, 2017: Do Statistical Pattern Corrections Improve Seasonal  
720 Climate Predictions in the North American Multimodel Ensemble Models? *Journal of*  
721 *Climate*, **30**, 8335–8355, <https://doi.org/10.1175/JCLI-D-17-0054.1>.
- 722 ———, ———, M. L. L’Heureux, S. Li, and D. G. DeWitt, 2012: Skill of Real-Time Seasonal  
723 ENSO Model Predictions during 2002–11: Is Our Capability Increasing? *Bulletin of the*  
724 *American Meteorological Society*, **93**, 631–651, [https://doi.org/10.1175/BAMS-D-11-](https://doi.org/10.1175/BAMS-D-11-00111.1)  
725 [00111.1](https://doi.org/10.1175/BAMS-D-11-00111.1).
- 726 Becker, E., H. van den Dool, and Q. Zhang, 2014: Predictability and Forecast Skill in NMME.  
727 *Journal of Climate*, **27**, 5891–5906, <https://doi.org/10.1175/JCLI-D-13-00597.1>.
- 728 Berner, J., H. M. Christensen, and P. D. Sardeshmukh, 2020: Does ENSO Regularity Increase in  
729 a Warming Climate? *Journal of Climate*, **33**, 1247–1259, [https://doi.org/10.1175/JCLI-D-](https://doi.org/10.1175/JCLI-D-19-0545.1)  
730 [19-0545.1](https://doi.org/10.1175/JCLI-D-19-0545.1).
- 731 Burger, F. A., J. Terhaar, and T. L. Frölicher, 2022: Compound marine heatwaves and ocean  
732 acidity extremes. *Nat Commun*, **13**, 4722, <https://doi.org/10.1038/s41467-022-32120-7>.
- 733 Cai, W., and Coauthors, 2021: Changing El Niño–Southern Oscillation in a warming climate.  
734 *Nat Rev Earth Environ*, **2**, 628–644, <https://doi.org/10.1038/s43017-021-00199-z>.
- 735 Capotondi, A., and Coauthors, 2015: Understanding ENSO diversity. *Bulletin of the American*  
736 *Meteorological Society*, **96**, 921–938, <https://doi.org/10.1175/BAMS-D-13-00117.1>.
- 737 Chen, D., M. A. Cane, A. Kaplan, S. E. Zebiak, and D. Huang, 2004: Predictability of El Niño  
738 over the past 148 years. *Nature*, **428**, 733–736, <https://doi.org/10.1038/nature02439>.
- 739 Delworth, T. L., and Coauthors, 2020: SPEAR: The Next Generation GFDL Modeling System  
740 for Seasonal to Multidecadal Prediction and Projection. *Journal of Advances in Modeling*  
741 *Earth Systems*, **12**, e2019MS001895, <https://doi.org/10.1029/2019MS001895>.
- 742 Derome, J., H. Lin, and G. Brunet, 2005: Seasonal Forecasting with a Simple General  
743 Circulation Model: Predictive Skill in the AO and PNA. *Journal of Climate*, **18**, 597–  
744 609, <https://doi.org/10.1175/JCLI-3289.1>.
- 745 Ding, H., M. Newman, M. A. Alexander, and A. T. Wittenberg, 2018: Skillful Climate Forecasts  
746 of the Tropical Indo-Pacific Ocean Using Model-Analogs. *Journal of Climate*, **31**, 5437–  
747 5459, <https://doi.org/10.1175/JCLI-D-17-0661.1>.

- 748 ———, ———, ———, and ———, 2019: Diagnosing Secular Variations in Retrospective ENSO  
749 Seasonal Forecast Skill Using CMIP5 Model-Analogs. *Geophysical Research Letters*, **46**,  
750 1721–1730, <https://doi.org/10.1029/2018GL080598>.
- 751 Gan, B., L. Wu, F. Jia, S. Li, W. Cai, H. Nakamura, M. A. Alexander, and A. J. Miller, 2017: On  
752 the Response of the Aleutian Low to Greenhouse Warming. *Journal of Climate*, **30**,  
753 3907–3925, <https://doi.org/10.1175/JCLI-D-15-0789.1>.
- 754 Gu, D., and S. G. H. Philander, 1997: Interdecadal climate fluctuations that depend on exchanges  
755 between the tropics and extratropics. *Science*, **275**, 805–807,  
756 <https://doi.org/10.1126/science.275.5301.805>.
- 757 He, S., J.-Y. Yu, S. Yang, and S.-W. Fang, 2020: ENSO’s impacts on the tropical Indian and  
758 Atlantic Oceans via tropical atmospheric processes: observations versus CMIP5  
759 simulations. *Clim Dyn*, **54**, 4627–4640, <https://doi.org/10.1007/s00382-020-05247-w>.
- 760 Heede, U. K., and A. V. Fedorov, 2023: Towards understanding the robust strengthening of  
761 ENSO and more frequent extreme El Niño events in CMIP6 global warming simulations.  
762 *Clim Dyn*, **61**, 3047–3060, <https://doi.org/10.1007/s00382-023-06856-x>.
- 763 Horel, J. D., and J. M. Wallace, 1981: Planetary-scale phenomena associated with the Southern  
764 Oscillation. *Mon. Wea. Rev.*, **109**, 813–829, [https://doi.org/10.1175/1520-0493\(1981\)109<0813:PSAPAW>2.0.CO;2](https://doi.org/10.1175/1520-0493(1981)109<0813:PSAPAW>2.0.CO;2).
- 766 Huang, B., and Coauthors, 2017: Extended reconstructed Sea surface temperature, Version 5  
767 (ERSSTv5): Upgrades, validations, and intercomparisons. *Journal of Climate*, **30**, 8179–  
768 8205, <https://doi.org/10.1175/JCLI-D-16-0836.1>.
- 769 Jacox, M. G., M. A. Alexander, C. A. Stock, and G. Hervieux, 2019: On the skill of seasonal sea  
770 surface temperature forecasts in the California Current System and its connection to  
771 ENSO variability. *Climate Dynamics*, **53**, 7519–7533, <https://doi.org/10.1007/s00382-017-3608-y>.
- 773 Kay, J. E., and Coauthors, 2015: The community earth system model (CESM) large ensemble  
774 project : A community resource for studying climate change in the presence of internal  
775 climate variability. *Bulletin of the American Meteorological Society*, **96**, 1333–1349,  
776 <https://doi.org/10.1175/BAMS-D-13-00255.1>.
- 777 Kirtman, B. P., and P. S. Schopf, 1998: Decadal Variability in ENSO Predictability and  
778 Prediction. *Journal of Climate*, **11**, 2804–2822, [https://doi.org/10.1175/1520-0442\(1998\)011<2804:DVIEPA>2.0.CO;2](https://doi.org/10.1175/1520-0442(1998)011<2804:DVIEPA>2.0.CO;2).
- 780 Kumar, A., 2009: Finite Samples and Uncertainty Estimates for Skill Measures for Seasonal  
781 Prediction. *Monthly Weather Review*, **137**, 2622–2631,  
782 <https://doi.org/10.1175/2009MWR2814.1>.
- 783 ———, P. Peng, and M. Chen, 2014: Is There a Relationship between Potential and Actual Skill?  
784 *Monthly Weather Review*, **142**, 2220–2227, <https://doi.org/10.1175/MWR-D-13-00287.1>.

- 785 Kumar, S., C. F. Dewes, M. Newman, and Y. Duan, 2023: Robust Changes in North America's  
786 Hydroclimate Variability and Predictability. *Earth's Future*, **11**, e2022EF003239,  
787 <https://doi.org/10.1029/2022EF003239>.
- 788 Kushnir, Y., W. A. Robinson, P. Chang, and A. W. Robertson, 2006: The Physical Basis for  
789 Predicting Atlantic Sector Seasonal-to-Interannual Climate Variability. *Journal of*  
790 *Climate*, **19**, 5949–5970, <https://doi.org/10.1175/JCLI3943.1>.
- 791 Lorenz, E. N., 1969: Atmospheric Predictability as Revealed by Naturally Occurring Analogues.  
792 *Journal of the Atmospheric Sciences*, **26**, 636–646, <https://doi.org/10.1175/1520->  
793 [0469\(1969\)26<636:APARBN>2.0.CO;2](https://doi.org/10.1175/1520-0469(1969)26<636:APARBN>2.0.CO;2).
- 794 Lou, J., M. Newman, and A. Hoell, 2023: Multi-decadal variation of ENSO forecast skill since  
795 the late 1800s. *npj Clim Atmos Sci*, **6**, 1–14, <https://doi.org/10.1038/s41612-023-00417-z>.
- 796 MacLeod, D., C. O'Reilly, T. Palmer, and A. Weisheimer, 2018: Flow dependent ensemble  
797 spread in seasonal forecasts of the boreal winter extratropics. *Atmospheric Science*  
798 *Letters*, **19**, e815, <https://doi.org/10.1002/asl.815>.
- 799 Maher, N., and Coauthors, 2019: The Max Planck Institute Grand Ensemble - Enabling the  
800 Exploration of Climate System Variability. *Journal of Advances in Modeling Earth*  
801 *Systems*, 2019MS001639, <https://doi.org/10.1029/2019MS001639>.
- 802 ———, S. Milinski, and R. Ludwig, 2021: Large ensemble climate model simulations:  
803 introduction, overview, and future prospects for utilising multiple types of large  
804 ensemble. *Earth System Dynamics*, **12**, 401–418, <https://doi.org/10.5194/esd-12-401->  
805 [2021](https://doi.org/10.5194/esd-12-401-2021).
- 806 ———, and Coauthors, 2023: The future of the El Niño–Southern Oscillation: using large  
807 ensembles to illuminate time-varying responses and inter-model differences. *Earth*  
808 *System Dynamics*, **14**, 413–431, <https://doi.org/10.5194/esd-14-413-2023>.
- 809 McGregor, S., C. Cassou, Y. Kosaka, and A. S. Phillips, 2022: Projected ENSO Teleconnection  
810 Changes in CMIP6. *Geophysical Research Letters*, **49**, e2021GL097511,  
811 <https://doi.org/10.1029/2021GL097511>.
- 812 Mo, K. C., and M. Ghil, 1987: Statistics and Dynamics of Persistent Anomalies. *Journal of the*  
813 *Atmospheric Sciences*, **44**, 877–902, <https://doi.org/10.1175/1520->  
814 [0469\(1987\)044<0877:SADOPA>2.0.CO;2](https://doi.org/10.1175/1520-0469(1987)044<0877:SADOPA>2.0.CO;2).
- 815 Newman, M., and P. D. Sardeshmukh, 2017: Are we near the predictability limit of tropical  
816 Indo-Pacific sea surface temperatures? *Geophysical Research Letters*, **44**, 8520–8529,  
817 <https://doi.org/10.1002/2017GL074088>.
- 818 O'Brien, J. P., and C. Deser, 2023: Quantifying and Understanding Forced Changes to Unforced  
819 Modes of Atmospheric Circulation Variability over the North Pacific in a Coupled Model  
820 Large Ensemble. *Journal of Climate*, **36**, 19–37, <https://doi.org/10.1175/JCLI-D-22->  
821 [0101.1](https://doi.org/10.1175/JCLI-D-22-0101.1).

- 822 O'Reilly, C. H., J. Heatley, D. MacLeod, A. Weisheimer, T. N. Palmer, N. Schaller, and T.  
823 Woollings, 2017: Variability in seasonal forecast skill of Northern Hemisphere winters  
824 over the twentieth century. *Geophysical Research Letters*, **44**, 5729–5738,  
825 <https://doi.org/10.1002/2017GL073736>.
- 826 ———, T. Woollings, L. Zanna, and A. Weisheimer, 2019: An Interdecadal Shift of the  
827 Extratropical Teleconnection From the Tropical Pacific During Boreal Summer.  
828 *Geophysical Research Letters*, **46**, 13379–13388,  
829 <https://doi.org/10.1029/2019GL084079>.
- 830 Power, S., and Coauthors, 2021: Decadal climate variability in the tropical Pacific:  
831 Characteristics, causes, predictability, and prospects. *Science*, **374**, eaay9165,  
832 <https://doi.org/10.1126/science.aay9165>.
- 833 Quan, X., M. Hoerling, J. Whitaker, G. Bates, and T. Xu, 2006: Diagnosing Sources of U.S.  
834 Seasonal Forecast Skill. *Journal of Climate*, **19**, 3279–3293,  
835 <https://doi.org/10.1175/JCLI3789.1>.
- 836 Rodgers, K. B., and Coauthors, 2021: Ubiquity of human-induced changes in climate variability.  
837 *Earth System Dynamics*, **12**, 1393–1411, <https://doi.org/10.5194/esd-12-1393-2021>.
- 838 Sardeshmukh, P. D., G. P. Compo, and C. Penland, 2000: Changes of Probability Associated  
839 with El Niño. *Journal of Climate*, **13**, 4268–4286, [https://doi.org/10.1175/1520-0442\(2000\)013<4268:COPAWE>2.0.CO;2](https://doi.org/10.1175/1520-0442(2000)013<4268:COPAWE>2.0.CO;2).
- 841 Scaife, A. A., and D. Smith, 2018: A signal-to-noise paradox in climate science. *npj Clim Atmos  
842 Sci*, **1**, 1–8, <https://doi.org/10.1038/s41612-018-0038-4>.
- 843 Shi, H., and Coauthors, 2022: Global decline in ocean memory over the 21st century. *Science  
844 Advances*, **8**, eabm3468, <https://doi.org/10.1126/sciadv.abm3468>.
- 845 Shi, W., N. Schaller, D. MacLeod, T. N. Palmer, and A. Weisheimer, 2015: Impact of hindcast  
846 length on estimates of seasonal climate predictability. *Geophysical Research Letters*, **42**,  
847 1554–1559, <https://doi.org/10.1002/2014GL062829>.
- 848 Storch, H. von, and F. W. Zwiers, 1999: *Statistical Analysis in Climate Research*. Cambridge  
849 University Press,.
- 850 Suarez, M. J., and P. S. Schopf, 1988: A Delayed Action Oscillator for ENSO. *Journal of the  
851 Atmospheric Sciences*, **45**, 3283–3287, [https://doi.org/10.1175/1520-0469\(1988\)045<3283:ADAOFE>2.0.CO;2](https://doi.org/10.1175/1520-0469(1988)045<3283:ADAOFE>2.0.CO;2).
- 853 Weisheimer, A., and T. N. Palmer, 2014: On the reliability of seasonal climate forecasts. *J R Soc  
854 Interface*, **11**, 20131162, <https://doi.org/10.1098/rsif.2013.1162>.
- 855 Weisheimer, A., N. Schaller, C. O'Reilly, D. A. MacLeod, and T. Palmer, 2017: Atmospheric  
856 seasonal forecasts of the twentieth century: multi-decadal variability in predictive skill of  
857 the winter North Atlantic Oscillation (NAO) and their potential value for extreme event

- 858 attribution. *Quarterly Journal of the Royal Meteorological Society*, **143**, 917–926,  
859 <https://doi.org/10.1002/qj.2976>.
- 860 —, D. Decremer, D. MacLeod, C. O’Reilly, T. N. Stockdale, S. Johnson, and T. N. Palmer,  
861 2019: How confident are predictability estimates of the winter North Atlantic  
862 Oscillation? *Quarterly Journal of the Royal Meteorological Society*, **145**, 140–159,  
863 <https://doi.org/10.1002/qj.3446>.
- 864 —, D. J. Bafort, D. MacLeod, T. Palmer, C. O’Reilly, and K. Strømmen, 2020: Seasonal  
865 Forecasts of the Twentieth Century. *Bulletin of the American Meteorological Society*,  
866 **101**, E1413–E1426, <https://doi.org/10.1175/BAMS-D-19-0019.1>.
- 867 —, M. A. Balmaseda, T. N. Stockdale, M. Mayer, S. Sharmila, H. Hendon, and O. Alves,  
868 2022: Variability of ENSO Forecast Skill in 2-Year Global Reforecasts Over the 20th  
869 Century. *Geophysical Research Letters*, **49**, e2022GL097885,  
870 <https://doi.org/10.1029/2022GL097885>.
- 871 Williams, I. N., and C. M. Patricola, 2018: Diversity of ENSO Events Unified by Convective  
872 Threshold Sea Surface Temperature: A Nonlinear ENSO Index. *Geophysical Research*  
873 *Letters*, **45**, 9236–9244, <https://doi.org/10.1029/2018GL079203>.
- 874 Wittenberg, A. T., A. Rosati, T. L. Delworth, G. A. Vecchi, and F. Zeng, 2014: ENSO  
875 Modulation: Is It Decadally Predictable? *Journal of Climate*, **27**, 2667–2681,  
876 <https://doi.org/10.1175/JCLI-D-13-00577.1>.
- 877 Zhao, M., H. H. Hendon, O. Alves, G. Liu, and G. Wang, 2016: Weakened Eastern Pacific El  
878 Niño Predictability in the Early Twenty-First Century. *Journal of Climate*, **29**, 6805–  
879 6822, <https://doi.org/10.1175/JCLI-D-15-0876.1>.
- 880 Zheng, Y., M. Rugenstein, P. Pieper, G. Beobide-Arsuaga, and J. Baehr, 2022: El Niño–Southern  
881 Oscillation (ENSO) predictability in equilibrated warmer climates. *Earth System*  
882 *Dynamics*, **13**, 1611–1623, <https://doi.org/10.5194/esd-13-1611-2022>.
- 883 Zhou, Z.-Q., S.-P. Xie, X.-T. Zheng, Q. Liu, and H. Wang, 2014: Global Warming–Induced  
884 Changes in El Niño Teleconnections over the North Pacific and North America. *Journal*  
885 *of Climate*, **27**, 9050–9064, <https://doi.org/10.1175/JCLI-D-14-00254.1>.
- 886